OPEN ACCESS

Catalysis & Surface ARTICLE

The Innovation Energy

CeO_2 facet-directed interfacial engineering in Ru_1/CeO_2 catalysts for efficient 2-butanol production from levulinic acid

Shaohua Zhang,[1,2] Fusen Liu,[1,2] Yuqi Zhang,[1] Wenguang Zhou,[1] Lungang Chen,[3,*] and Yong Liu[1,*]

*Correspondence: liuyongncu@ncu.edu.cn (Yong Liu); chenlg@seu.edu.cn (Lungang Chen)

Received: February 24, 2026; Accepted: April 13, 2026; Published Online: April 20, 2026; https://doi.org/10.59717/j.xinn-energy.2026.100156

GRAPHICAL ABSTRACT

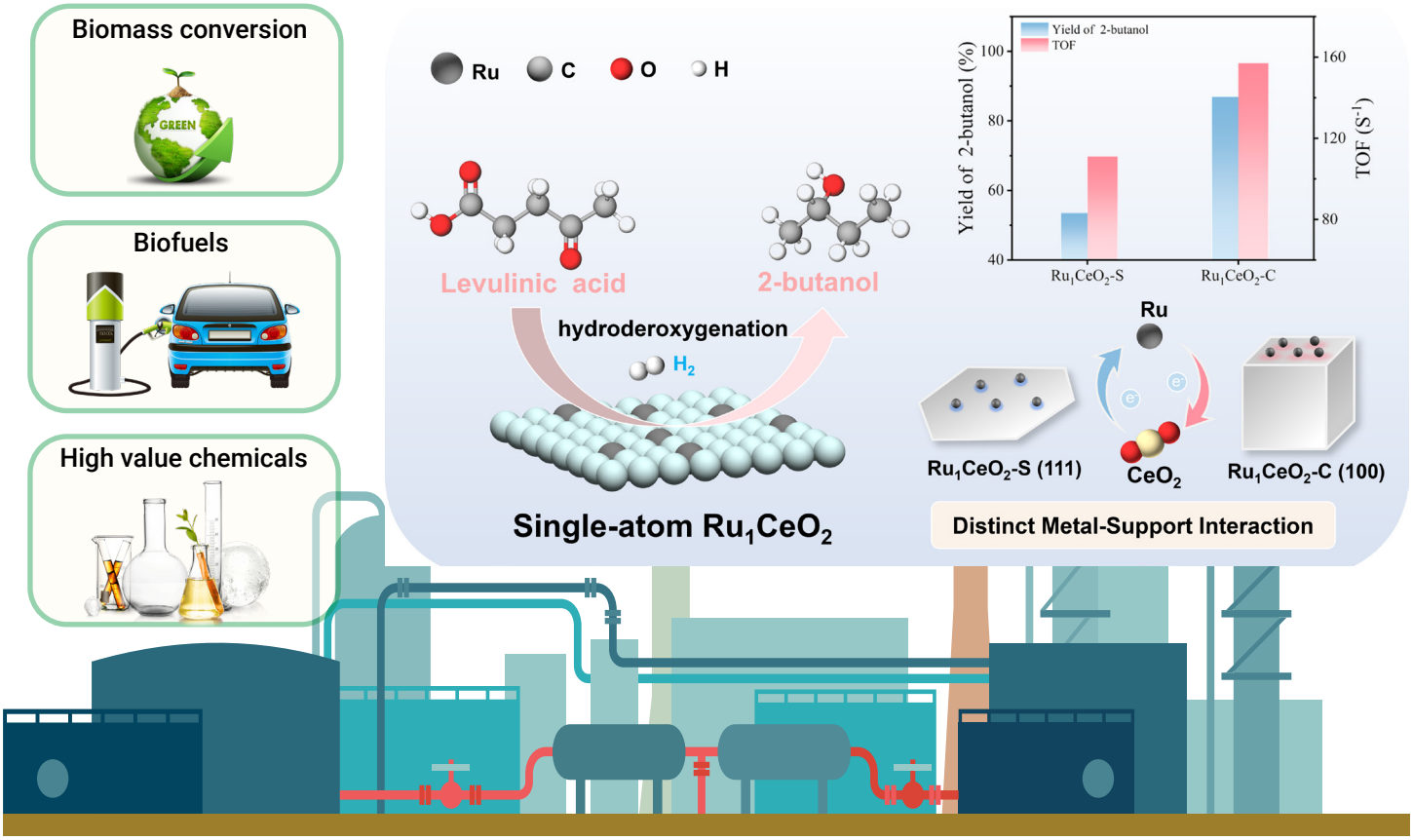

PUBLIC SUMMARY

- Facet-engineered CeO_2 supports tune single-atom Ru catalysts for biomass conversion.
- Ru_1/CeO_2-C achieves 86.9% yield of 2-butanol with high catalytic activity.
- (100) facets create more oxygen vacancies and stronger metal–support interactions.
- Enhanced hydrogen transfer and C–C cleavage improve reaction efficiency.
- Provides a strategy to design high-performance catalysts for biomass upgrading.

ARTICLE Catalysis & Surface

OPEN ACCESS

CeO_2 facet-directed interfacial engineering in Ru_1/CeO_2 catalysts for efficient 2-butanol production from levulinic acid

Shaohua Zhang,[1,2] Fusen Liu,[1,2] Yuqi Zhang,[1] Wenguang Zhou,[1] Lungang Chen,[3,*] and Yong Liu[1,*]

[1]School of Resources & Environment and Key Laboratory of Poyang Lake Environment and Resource Utilization, Ministry of Education, Nanchang University, Nanchang 330047, China

[2]School of Physics and Materials Science, Nanchang University, Nanchang 330047, China

[3]Key Laboratory of Energy Thermal Conversion and Control of Ministry of Education, School of Energy and Environment, Southeast University, Nanjing 210096, China

*Correspondence: liuyongncu@ncu.edu.cn (Yong Liu); chenlg@seu.edu.cn (Lungang Chen)

Received: February 24, 2026; Accepted: April 13, 2026; Published Online: April 20, 2026; https://doi.org/10.59717/j.xinn-energy.2026.100156

Citation: Zhang S., Liu F., Zhang Y., et al. (2026). CeO_2 facet-directed interfacial engineering in Ru_1/CeO_2 catalysts for efficient 2-butanol production from levulinic acid. *The Innovation Energy* **3**:100156.

Optimizing the selectivity of biomass-derived platform chemicals requires precise control over the geometric and electronic structures of catalytic active sites. Herein, we report the structural engineering of single-atom ruthenium (Ru_1) supported on ceria (CeO_2) nanocrystals with distinct crystal facets to regulate the hydrodeoxygenation of levulinic acid to 2-butanol. Using a facile photodeposition method, Ru_1 species were anchored onto cubic (CeO_2-C, exposing (1 0 0) facets) and sheet-like (CeO_2-S, exposing (1 1 1) facets) supports. The Ru_1CeO_2-C catalyst exhibited superior catalytic performance, achieving an 86.9% yield of 2-butanol at 190 °C with a turnover frequency value of 157 s^{-1}, surpassing the Ru_1CeO_2-S catalyst (53.5% and 111 s^{-1}). Comprehensive characterization, including XPS, Raman spectroscopy, and EPR, revealed that the (1 0 0) facets of CeO_2-C facilitate a higher concentration of surface oxygen vacancies and foster the electronic metal-support interaction. This interaction stabilizes Ru species and promotes the formation of Lewis acid sites, which are critical for the ring-opening of the key intermediate, γ-valerolactone. Kinetic studies, *in situ* DRIFTS, and theoretical calculations further confirmed that the facet-dependent electronic structure of Ru_1CeO_2-C significantly enhances hydrogen transfer capabilities and C-C bond cleavage efficiency. This work elucidates the structure-activity relationship in single-atom catalysis and offers a facet-engineering strategy for designing efficient biomass conversion catalysts.

INTRODUCTION

The transition from fossil resources to renewable biomass for the production of fuels and chemicals is a pivotal step toward global energy security and carbon neutrality.[1,2] Levulinic acid (LA), a primary platform molecule derived from cellulose degradation, has garnered significant attention due to its potential to be converted into high-value derivatives.[3] Among these, 2-butanol (2-BuOH), produced via the hydrodeoxygenation (HDO) of LA, is particularly valuable as a fuel additive, solvent, and chemical intermediate.[4,5] However, the selective synthesis of 2-BuOH is kinetically challenging; it requires a multifunctional catalyst capable of activating molecular hydrogen, suppressing side reactions, and facilitating sequential hydrogenation and C-C bond cleavage steps.[6,7]

Recent advances have demonstrated the efficacy of metal-acid bifunctional catalysts for this transformation (Table S1). For instance, nickel-based systems utilizing Ni-Mn synergy have achieved yields up to 84.5%[6], while ruthenium-based catalysts, including nanoporous Ru and Ru-Mn systems, have shown promising activity by balancing hydrogenation and deoxygenation functions.[7-10] Nanoporous Ru achieved a 63.6% 2-butanol yield by activating the lactone group of γ-valerolactone (GVL) and the C-C/C-O bond of 1,4-pentanediol (1,4-PDO),[8] and the Ru/CeO_2 catalyst can achieve a yield of 85% for the hydrogenation deoxidation of LA in the aqueous phase.[9] The addition of Mn in $Ru_{3.75}Mn_{15}/Al_2O_3$ achieves a metal-acid bifunctional synergy (Ru^0 hydrogenation and Mn^{2+} deoxidation) and an oxygen vacancy effect.[10] While high Ru loading or bimetallic alloying has been effective in modulating electronic structures, the role of the support's surface geometry—specifically the exposed crystal facets—in regulating single-atom active sites remains under-explored in the context of LA conversion.

Cerium oxide (CeO_2) is a widely used support due to its exceptional oxygen storage capacity and redox properties.[11-13] The catalytic behavior of CeO_2 is inherently structure-sensitive; different morphologies (cubes, rods, sheets) expose distinct crystal planes with varying oxygen vacancy formation energies and surface coordinations.[14] Previous studies on oxidation reactions have established that specific facets, such as the (1 0 0) planes in nanocubes or (1 1 0) in nanorods, can significantly alter metal-support interactions and oxygen vacancy concentrations.[15-17] However, a systematic understanding of how these facet-dependent properties influence the complex hydrodeoxygenation pathway of LA over single-atom Ru catalysts is currently lacking.

In this study, we address this gap by synthesizing single-atom Ru_1CeO_2 catalysts with controlled morphologies—nanosheets (CeO_2-S) and nanocubes (CeO_2-S)—via a photodeposition method. We investigate the distinct physicochemical properties arising from the exposed (1 1 1) and (1 0 0) facets, respectively. Our results demonstrate that the Ru_1CeO_2-C catalyst, exposing (1 0 0) facets, achieves a superior 2-BuOH yield of 86.9% and turnover frequency (TOF) value of 157 s^{-1}. Through detailed kinetic analysis and in situ characterization, we reveal that the (1 0 0) facet promotes a high density of oxygen vacancies and stabilizes Ru species, thereby enhancing Lewis acidity and hydrogen transfer efficiency. These findings provide a rational strategy for optimizing single-atom catalysts through interfacial structural engineering for sustainable biomass valorization.

MATERIALS AND METHODS

Materials

$Ce(NO_3)_3{\cdot}6H_2O$ (99%), NH_4HCO_3 (99.99%), $RuCl_3{\cdot}xH_2O$, ethanol (EtOH, 99.7%), isopropanol (IPA, 99.5%), acetone (99.5%), 2-BuOH (99%), 2-pentanol (2-PeOH, 98%), 5-hydroxy-2-pentanone (HPO, 95%), 1,4-PDO (98%), GVL (98%), LA (99%), methyl levulinate (ML, 98%), ethyl levulinate (EL, 99%), propyl levulinate (PL, 98%), and butyl levulinate (BL, 98%) were purchased from Macklin Inc. All chemicals were used as received without further purification.

Synthesis of Ru_1CeO_2 catalysts

Synthesis of CeO_2-C (Cubic, (1 0 0) facet-dominant). CeO_2-C nanocubes, primarily exposing the (1 0 0) facets, were synthesized using a hydrothermal method.[18] Typically, 1.37 g $Ce(NO_3)_3{\cdot}6H_2O$ and 11.82 g NaOH were dissolved in 32 ml and 24 mL deionized water, respectively. The NaOH solution was added dropwise to the $Ce(NO_3)_3{\cdot}6H_2O$ solution under continuous stirring for 30 min. The resulting suspension was transferred to a 100 mL Teflon-lined stainless-steel autoclave and heated at 180 °C for 24 h. After cooling, the precipitate was collected by centrifugation, washed thoroughly with deionized water and absolute ethanol several times, and dried overnight at 80 °C. The resulting powder was then calcined in air at 500 °C for 4 h (heating rate: 2 °C/min) to obtain the CeO_2-C support.

Synthesis of CeO_2-S (Sheet-like, (1 1 1) facet-dominant). CeO_2-S nanosheets, predominantly exposing the (1 1 1) facets, were synthesized following a precipitation method.[19] Typically, 1.39 g $Ce(NO_3)_3{\cdot}6H_2O$ and 0.75g NH_4HCO_3 were successively dissolved in 200 mL deionized water under vigorous stirring for 30 min. The resulting mixed solution was transferred into sealed beakers and maintained at 25 °C for 24 h. The obtained precipitates were collected by centrifugation, thoroughly washed with distilled water, and dried at 50 °C for 12 h. Finally, the dried solid was calcined in a muffle furnace at 450 °C for 8 h to afford CeO_2-S.

Synthesis of Ru_1CeO_2 catalysts. The Ru_1CeO_2 catalyst was synthesized via a facile photodeposition method. Briefly, 0.6 g pre-synthesized CeO_2 was dispersed in 60 mL deionized water under continuous stirring. An aqueous solution of $RuCl_3{\cdot}H_2O$ was then slowly added to the suspension. After stirring for 10 min, the mixture was transferred to a 100 mL thick-walled reactor. Dissolved air was removed by purging with nitrogen, after which the suspension was irradiated with a 30 W UV lamp (λ = 370 nm) for 24 h under continuous stirring. The resulting solid was collected, thoroughly washed with deionized water and ethanol, and dried at 60 °C overnight. By varying the CeO_2 support, Ru_1CeO_2-C and Ru_1CeO_2-S catalysts with distinct morphologies were successfully obtained.

Catalyst characterizations

Details on X-ray diffraction (XRD) analysis, N_2-sorption, Inductively coupled plasma mass spectrometry (ICP-MS) Scanning electron microscopy (SEM), Transmission electron microscopy (TEM), High-angle annular dark-field microscopy (HAADF), Ru K-edge XAFS analyses, Raman spectroscopy test, X-ray photoelectron spectroscopy (XPS) measurements, Electron paramagnetic resonance (EPR), UV-Vis diffuse reflectance spectroscopy (UV-Vis DRS), Pyridine Fourier transform infrared spectroscopy (Py-FTIR), thermal-gravimetric analysis (TGA), and *in situ* diffuse reflectance infrared Fourier transform spectroscopy (DRIFTS) tests are given in the supporting information.

Catalytic performance test

The catalytic performance of Ru_1CeO_2 catalysts with different exposed crystal facets was evaluated for the hydrodeoxygenation of LA in a 50 mL stainless-steel autoclave. In a typical reaction, 140 mg LA and 70 mg catalyst were dispersed in 8.65 mL IPA. The reactor was sealed, purged with H_2 five times, pressurized to 5 MPa, and heated to 190 °C. The reaction was conducted under magnetic stirring at 400 rpm for 8 h. After completion, the reactor was cooled to room temperature, and the reaction mixture was filtered to remove the catalyst. The liquid products were analyzed using a Shimadzu GC-2014C gas chromatograph equipped with an HP-INNOWAX capillary column (30 m × 0.25 mm × 0.25 μm). The LA conversion, product yield, turnover number (TON), and TOF (substrate conversion < 30%) were calculated using the following equations:

$$Conversion(\%) = \frac{n_{LA,initial} - n_{LA,final}}{n_{LA,initial}} \times 100\% \quad (1)$$

$$Product\ yield(\%) = \frac{n_{product}}{n_{LA,initial}} \times 100\% \quad (2)$$

$$TON = \frac{n_{2-BuOH}}{n_{Ru}} \times 100\% \quad (3)$$

$$TOF = \frac{Substrate\ conversion\ rate}{n_{Ru}} \times 100\% \quad (4)$$

Catalyst reusability was evaluated through three consecutive reaction cycles. GVL was used as the substrate instead of LA, as LA was rapidly and completely converted to GVL under the reaction conditions. Each cycle was performed with 140 mg GVL, 70 mg catalyst, and 8.65 mL IPA at 190 °C and 5 MPa H_2 for 8 h. After each run, the catalyst was recovered by centrifugation, washed six times with ethanol and deionized water, and dried at 60 °C overnight before reuse.

DFT calculations

Two simplified slab models were constructed: (i) Ru_1CeO_2-S(111), consisting of a four-layer slab (95 atoms; $Ru_1Ce_{31}O_{63}$) with a single Ru atom anchored on the CeO_2(1 1 1) surface and one adjacent oxygen vacancy; and (ii) Ru_1CeO_2-C(100), consisting of a three-layer slab (143 atoms; $Ru_1Ce_{47}O_{95}$) with a single Ru atom anchored on the CeO_2(1 0 0) surface and one adjacent oxygen vacancy. In all models, the bottom two layers were fixed, while the remaining atoms were fully relaxed. A vacuum layer of 20 Å was introduced along the z direction to minimize interactions between periodic images. Additional computational details are provided in the supporting information.

RESULTS

Catalyst characterizations

The synthesis of CeO_2 supports with controlled crystal facets was achieved via hydrothermal and precipitation methods, followed by the anchoring of single-atom ruthenium species using a facile photodeposition strategy (Figure 1A). XRD patterns (Figure 1B) for both the cubic (Ru_1CeO_2-C) and sheet-like (Ru_1CeO_2-S) catalysts exhibited diffraction peaks of the typical CeO_2 structure (PDF No. 34-0394).[20,21] Notably, no diffraction peaks corresponding to metallic Ru or RuO_x species were detected, suggesting that the ruthenium species are highly dispersed on the support surfaces.

Textural properties, including specific surface area, pore volume, and pore size distribution, were examined. As shown in Figure 1C&D, both Ru_1CeO_2-C and Ru_1CeO_2-S exhibit type IV N_2-sorption isotherms with pronounced H3 hysteresis loops, characteristic of mesoporous structures.[22,23] Although the two catalysts possess comparable specific surface areas (50.2 and 55.5 $m^2\ g^{-1}$ for Ru_1CeO_2-C and Ru_1CeO_2-S, respectively; Table S2), their pore structures differ markedly. Ru_1CeO_2-C shows a much larger pore volume (0.32 $cm^3\ g^{-1}$) and average pore diameter (21.3 nm) than Ru_1CeO_2-S (0.051 $cm^3\ g^{-1}$ and 4.18 nm). The enlarged pore volume and pore size of the cubic catalyst are favorable for mass transfer of reactants and products, which is consistent with its superior catalytic performance.

The morphology and microstructure of the catalysts were further examined by SEM, TEM, AC-HAADF-STEM, and elemental mapping. As shown in Figure 1E-G, Ru_1CeO_2-C exhibits a well-defined cubic morphology with an average particle size of 20.78 ± 6.78 nm. The measured lattice spacing of 0.27 nm corresponds to the CeO_2(1 0 0) plane.[24] In contrast, Ru_1CeO_2-S displays a lamellar nanosheet morphology with a larger lateral size, and a lattice spacing of 0.31 nm characteristic of the CeO_2(1 1 1) plane (Figure 1H-J).[25] ICP-MS analysis (Table S2) confirmed success loading of Ru species. AC-HAADF-STEM image and elemental mappings (Figure 1K&L) suggested the uniform distribution of Ru species on both catalysts, consistent with highly dispersed, single-atom Ru sites.

To unequivocally verify the single-atom nature of Ru species, *in situ* CO-DRIFTS and synchrotron-based X-ray absorption characterization were performed.[26,27] As shown in Figure 2A&B, distinct absorption bands at approximately 2055 and 2020 cm^{-1} are observed for both Ru_1CeO_2 catalysts, which are characteristic of linearly adsorbed CO on isolated Ru atoms.[28,29] Ru K-edge XANES spectra (Figure 2C) reveal that the absorption edges of Ru_1CeO_2-C and Ru_1CeO_2-S lie between those of Ru foil and RuO_2,[30] with near-edge features resembling RuO_2, indicating that the average oxidation state of Ru is between 0 and +4. EXAFS analysis (Figure 2D) shows a dominant scattering peak at ~1.46 Å for Ru_1CeO_2-C and ~1.48 Å for Ru_1CeO_2-S, corresponding to Ru-O coordination, while no Ru–Ru contribution is detected, in sharp contrast to the Ru foil reference.[31] Quantitative fitting (Figures 2E&S1; Table S3) yields average Ru-O coordination numbers of 4.2 and 3.9 for Ru_1CeO_2-C and Ru_1CeO_2-S, respectively. WT-EXAFS analysis (Figures 2F-I & S2) further confirms that only Ru-O coordination exists in both catalysts.

The work function of Ru_1CeO_2 provides important insight into facet-dependent electronic metal–support interactions. CeO_2(1 1 1), possessing a relatively low work function, facilitates electron transfer from the support to Ru atoms, leading to a lower Ru oxidation state. In contrast, CeO_2(1 0 0) exhibits a higher work function, which suppresses electron transfer and stabilizes Ru in a more oxidized state (Figure 2H&I). This facet-dependent electronic modulation is fully consistent with the Ru 3p XPS results.

XPS, Raman spectroscopy, and EPR were comprehensively employed to investigate the surface structure and oxygen vacancy concentration of Ru_1CeO_2 catalysts, with particular emphasis on the influence of exposed CeO_2 crystal facets. The Ce 3d spectra (Figure 3A) can be deconvoluted into eight characteristic peaks, where the v' and u' components correspond to Ce^{3+} species, while the remaining peaks are assigned to Ce^{4+} [32]. The Ce^{3+} content (Table S4) follows the order Ru_1CeO_2-C (20%) > Ru_1CeO_2-S (17%), indicating a possible higher concentration of oxygen vacancies on the cubic catalyst.

The O 1s XPS spectra (Figure 3B) were deconvoluted to three peaks: lattice oxygen (O_α, 529.2 eV), oxygen species associated with oxygen vacancies (O_β, 530.2 eV), and weakly bound surface oxygen species (O_γ, 532.1 eV).[15,33,34] The concentration of oxygen vacancies (Table S4) exhibits the trend: Ru_1CeO_2-C (34%) > Ru_1CeO_2-S (28%). This consistency with the Ce^{3+} analysis confirms

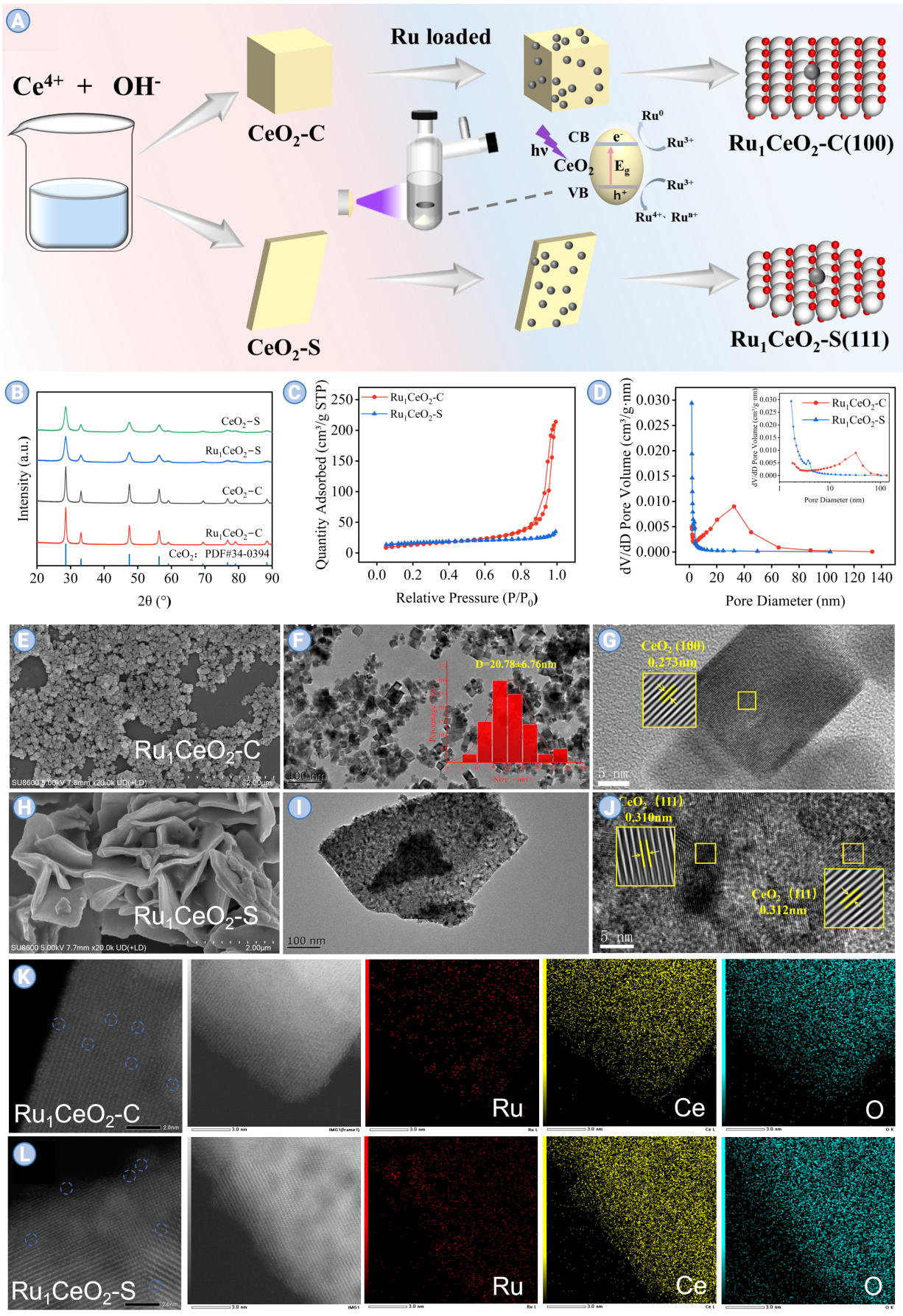

Figure 1. (A) Schematic illustration of the preparation process for Ru_1CeO_2 catalysts via facet engineering and photodeposition. (B) XRD patterns of CeO_2 supports and Ru_1CeO_2 catalysts. (C) N_2-sorption isotherms and (D) pore size distribution curves of catalysts. (E) SEM images, (F&G) TEM images, and (k) AC-HAADF-STEM image and elemental mapping of Ru_1CeO_2-C. (H) SEM images, (I&J) TEM images, and (l) AC-HAADF-STEM image and elemental mapping of Ru_1CeO_2-S.

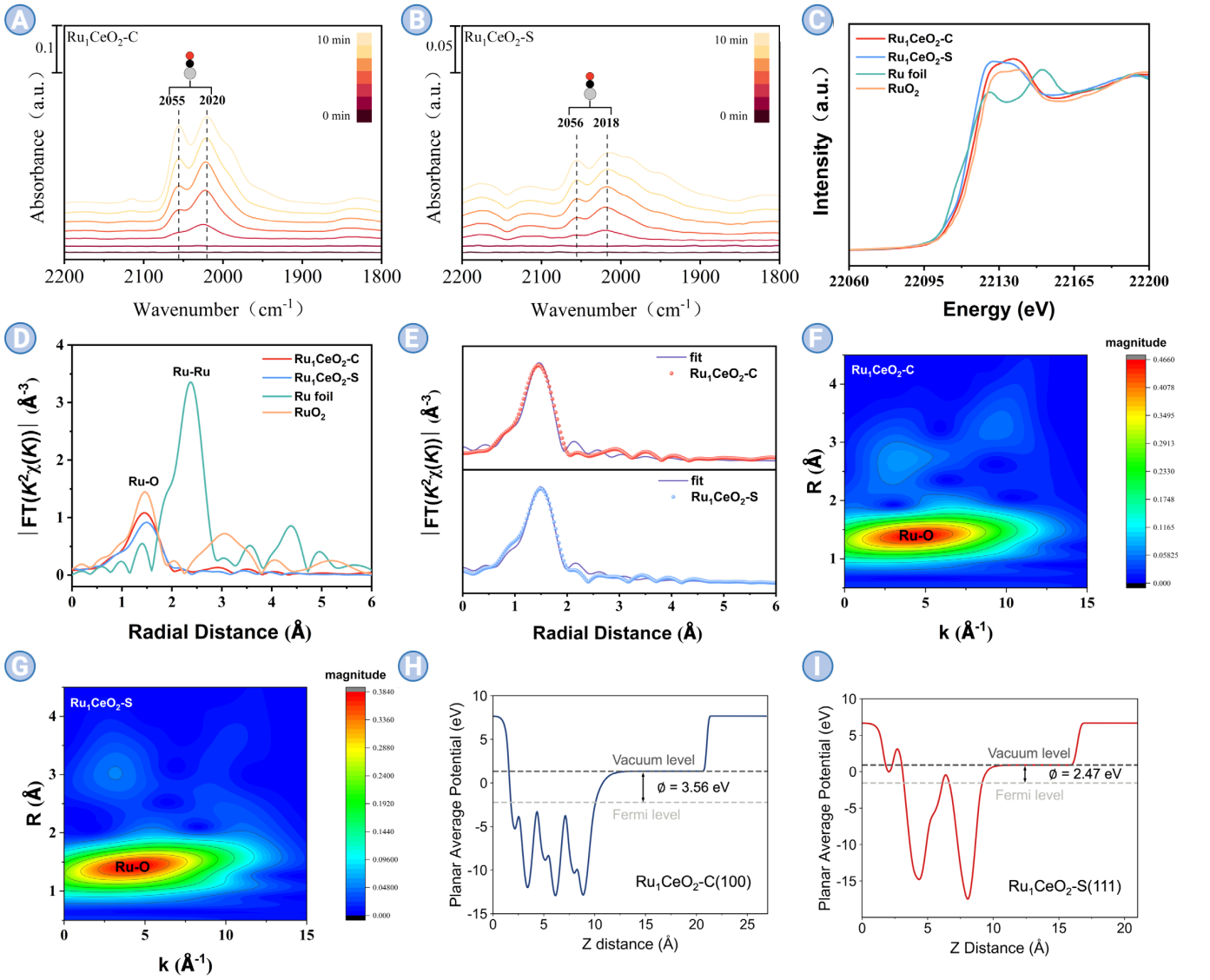

Figure 2. ***In situ*** **CO-DRIFTS of (A) Ru_1CeO_2-C and (B) Ru_1CeO_2-S. (C) Ru K-edge XANES spectra and (D) FT-EXAFS spectra of Ru_1CeO_2-C and Ru_1CeO_2-S, with Ru foil and RuO_2 provided as references. (E) EXAFS fitting curves at the Ru K-edge for both catalysts. R-space fitting results of the EXAFS spectra for (F) Ru_1CeO_2-C and (G) Ru_1CeO_2-S. Calculated work functions of (H) Ru_1CeO_2-C and (I) Ru_1CeO_2-S.**

that Ru_1CeO_2-C possesses the highest oxygen vacancy density. The higher vacancy concentration is attributed to the preferential exposure of the CeO_2(1 0 0) facet in Ru_1CeO_2-C, which has a lower oxygen vacancy formation energy than the CeO_2(1 1 1) facet predominantly exposed in Ru_1CeO_2-S.[35,36]

For comparison, the pure CeO_2-C support exhibits significantly lower Ce^{3+} (17%) and O_β (18%) contents than Ru_1CeO_2-C, demonstrating that Ru anchoring further promotes oxygen vacancy formation through electronic metal–support interaction (EMSI). The Ru 3p spectra (Figure 3C) consist of Ru $3p_{3/2}$ and $3p_{1/2}$, which can be deconvoluted into Ru^0, Ru^{4+}, and Ru^{n+} species, confirming that Ru predominantly exists in oxidation states. The precursor Ru^{3+} was reduced/oxidized by the photogenerated electrons/holes during the photodeposition process. Notably, the $Ru^{\delta+}/(Ru^{\delta+} + Ru^0)$ ($Ru^{\delta+}$: Ru^{4+} and Ru^{n+}) ratio follows the order Ru_1CeO_2-C (79%) > Ru_1CeO_2-S (70%), indicating a higher proportion of Ru-O-Ce coordination in Ru_1CeO_2-C. Moreover, Based on the binding energy analysis results, the binding energy peaks of Ru^{n+} and Ru^{4+} in the Ru_1CeO_2-S catalyst (488.4 and 466.8 eV; 483.7 and 463.5 eV) exhibit a negative shift compared to those in the Ru_1CeO_2-C catalyst (488.5 and 467.2 eV; 486 and 463.7 eV).[37] This indicates that Ru_1CeO_2-S facilitates electron transfer from the support to Ru, making Ru more electron-rich and reducing its oxidation state, whereas Ru_1CeO_2-C inhibits this electron transfer process, maintaining Ru in a relatively higher oxidation state.[38,39] This variation in the electronic structure of Ru species reflects the distinct EMSI in the two catalysts.

Raman spectroscopy further corroborates the facet-dependent oxygen vacancy concentration. As shown in Figure 3D, characteristic bands at ~454, 587, and 1170 cm^{-1} correspond to the F_{2g} mode of fluorite CeO_2, defect-induced (D) mode, and second-order longitudinal optical (2LO) mode, respectively.[40,41] The intensity ratio $I_D/(I_{F2g} + I_{2LO})$, commonly used to estimate oxygen vacancy concentration, is 5.2% for Ru_1CeO_2-C and only 1.9% for Ru_1CeO_2-S, confirming the significantly higher defect density in the cubic catalyst. Moreover, additional bands at ~692 and 984 cm^{-1} are assigned to Ru-O-Ce vibrational modes,[42,43] providing direct evidence for the formation of strong Ru-O-Ce interfacial structures in Ru_1CeO_2-C. These features are scarcely observed in Ru_1CeO_2-S, indicating weaker metal–support interactions on the (1 1 1) facet.

EPR spectroscopy (Figure 3E) reveals a characteristic signal at g = 2.003, corresponding to paramagnetic oxygen vacancy defects. The signal intensity follows the order Ru_1CeO_2-C > Ru_1CeO_2-S > CeO_2-C, in excellent agreement with the trends observed by XPS and Raman spectroscopy, thereby providing independent confirmation that Ru_1CeO_2-C possesses the highest oxygen vacancy concentration.

Py-FTIR spectroscopy was employed to probe the acidity of Ru_1CeO_2 catalysts (Figure 3F & Table S5). Bands at 1593 and 1447 cm^{-1} are assigned to

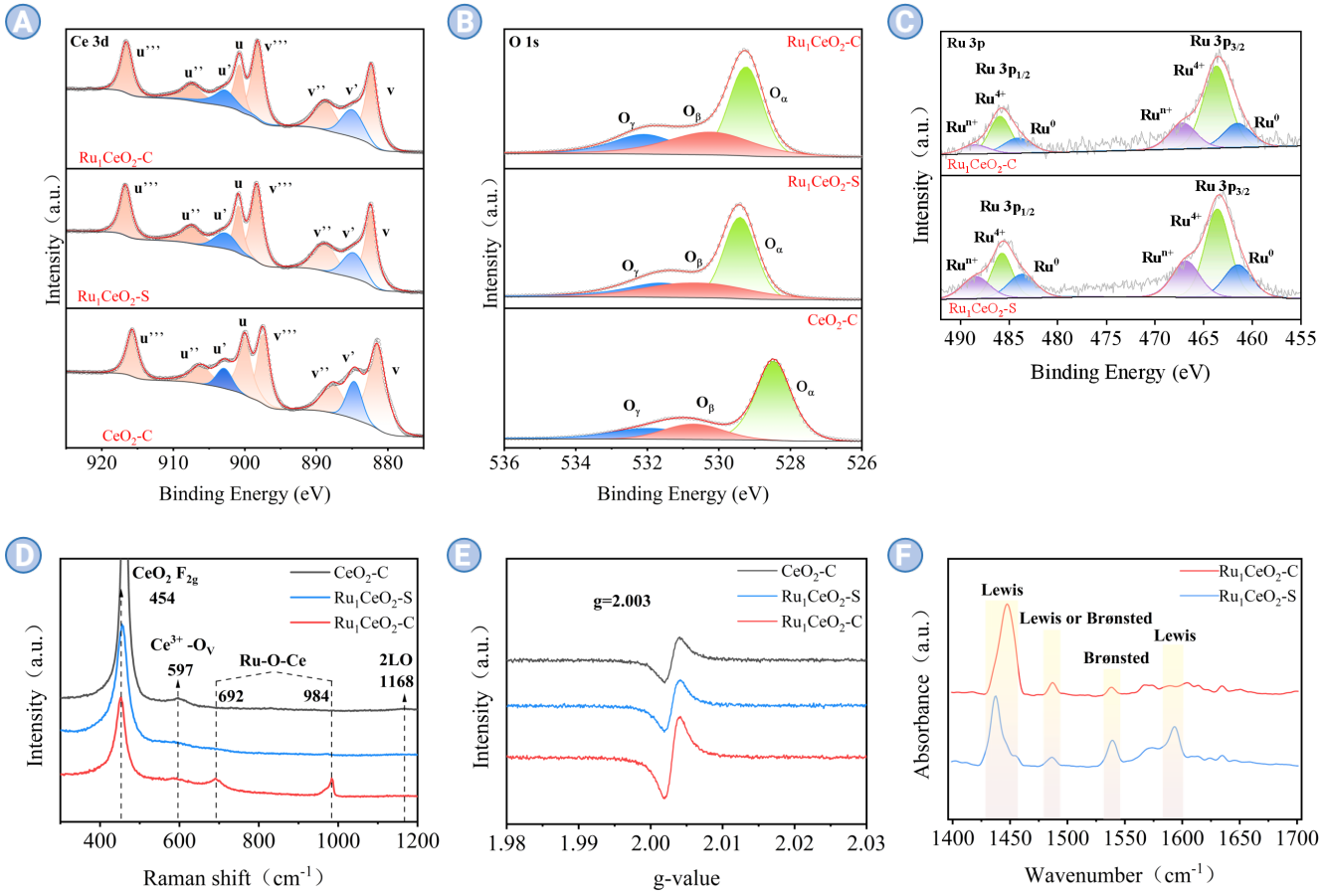

Figure 3. (A) Ce 3d XPS spectra, (B) O 1s XPS spectra, (C) Ru 3p XPS spectra, (D) Raman spectra, (E) EPR spectra, and (F) Py-FTIR spectra of samples.

Lewis acid sites, the band at 1539 cm^{-1} corresponds to Brønsted acid sites, and the band at 1487 cm^{-1} is associated with combined Lewis–Brønsted acidity[44]. Quantitative analysis shows that Ru_1CeO_2-C possesses a substantially higher concentration of Lewis acid sites but fewer Brønsted acid sites than Ru_1CeO_2-S. The enrichment of Lewis acid sites is beneficial for the ring-opening of the key intermediate GVL, thereby enhancing the selectivity toward 2-butanol.

Lewis acid sites in CeO_2-based catalysts are closely correlated with oxygen vacancies.[45,46] Combined XPS, Raman, and EPR results confirm that the high density of oxygen vacancies in Ru_1CeO_2-C provides the structural basis for its abundant Lewis acidity. In addition, Lewis acidity is influenced by the loading amount and oxidation state of Ru species.[7,47] The Ru_1CeO_2-C exhibits the slightly higher actual Ru loading (0.87 wt%). The EMSI stabilizes a higher fraction of $Ru^{\delta+}$ species, which themselves act as Lewis acid sites. The synergistic interaction between $Ru^{\delta+}$ centers and adjacent oxygen vacancies generates highly active Lewis acid ensembles, ultimately accounting for the superior catalytic performance of Ru_1CeO_2-C in levulinic acid hydrodeoxygenation, as discussed in the following section.

Catalytic performance

The catalytic performance of Ru_1CeO_2 catalysts was evaluated using LA and its key intermediates as substrates under conditions of 190 °C, 5 MPa H_2, and 8 h (Figures 4 & S3). As shown in Figure 4B, both CeO_2-C and CeO_2-S supports without Ru loading exhibit negligible catalytic activity, producing mainly GVL with trace amounts of HPO and 1,4-PDO. After loading 1 wt% Ru, the catalytic activities of both materials increased dramatically, confirming the essential role of Ru species. Among the catalysts, Ru_1CeO_2-C displays the best performance, achieving complete LA conversion with a 2-butanol yield of 86.9%, whereas Ru_1CeO_2-S affords only a 53.5% yield under identical conditions. Other than these products, trace amounts of 2-pentanol were observed in high pressure of 5 MPa H_2. Time-dependent product distributions (Figure 4C&D) reveal that GVL is the dominant intermediate over both catalysts, indicating that the subsequent hydrogenolysis of GVL is the rate-determining step for 2-butanol formation.

To further elucidate the kinetic behavior, apparent reaction orders were determined for the hydrogenolysis of GVL. As shown in Figure 4E, the reaction orders with respect to GVL concentration are 1.28 for Ru_1CeO_2-C and 1.21 for Ru_1CeO_2-S. This strong dependence suggests that the reaction rate is highly sensitive to GVL surface coverage. In contrast, the apparent reaction orders with respect to H_2 during GVL hydrodeoxygenation are relatively low (0.23 for Ru_1CeO_2-C and 0.15 for Ru_1CeO_2-S; Figure 4F), indicating that hydrogen adsorption is nearly saturated under the reaction conditions. Notably, in the hydrogenolysis of 1,4-PDO (Figure 4G), the H_2 reaction orders increased markedly to 0.80 for Ru_1CeO_2-C and 0.59 for Ru_1CeO_2-S, approaching first-order kinetics. This result suggests that the C-C bond cleavage in 1,4-PDO is more strongly dependent on hydrogen availability, highlighting a mechanistic distinction between GVL hydrodeoxygenation and deeper hydrogenation steps toward 2-butanol.

Consistent with the kinetic analysis, Ru_1CeO_2-C exhibits excellent activity for the conversion of key intermediates, including GVL, HPO, and 1,4-PDO, achieving 2-butanol yields exceeding 80% and TONs above 240 in all cases (Figure 4H). In contrast, Ru_1CeO_2-S shows significantly inferior performance (2-butanol yields < 25% and TONs < 60). Furthermore, Ru_1CeO_2-C demonstrates broad applicability for the hydrodeoxygenation of levulinates, including methyl, ethyl, propyl, and butyl levulinates, all of which are efficiently converted to 2-butanol (Figure 4I). The effects of UV irradiation time during catalyst synthesis, reaction temperature, and solvent on catalytic performance were systematically investigated (Figure S3). The optimal conditions correspond to a UV irradiation time of 24 h and reaction temperature of 190 °C. Deviations from the optimal reaction temperature in either direction led to a decrease in 2-butanol yield, indicating the necessity of balancing hydrogenation and hydrogenolysis steps. Without the present of H_2, IPA

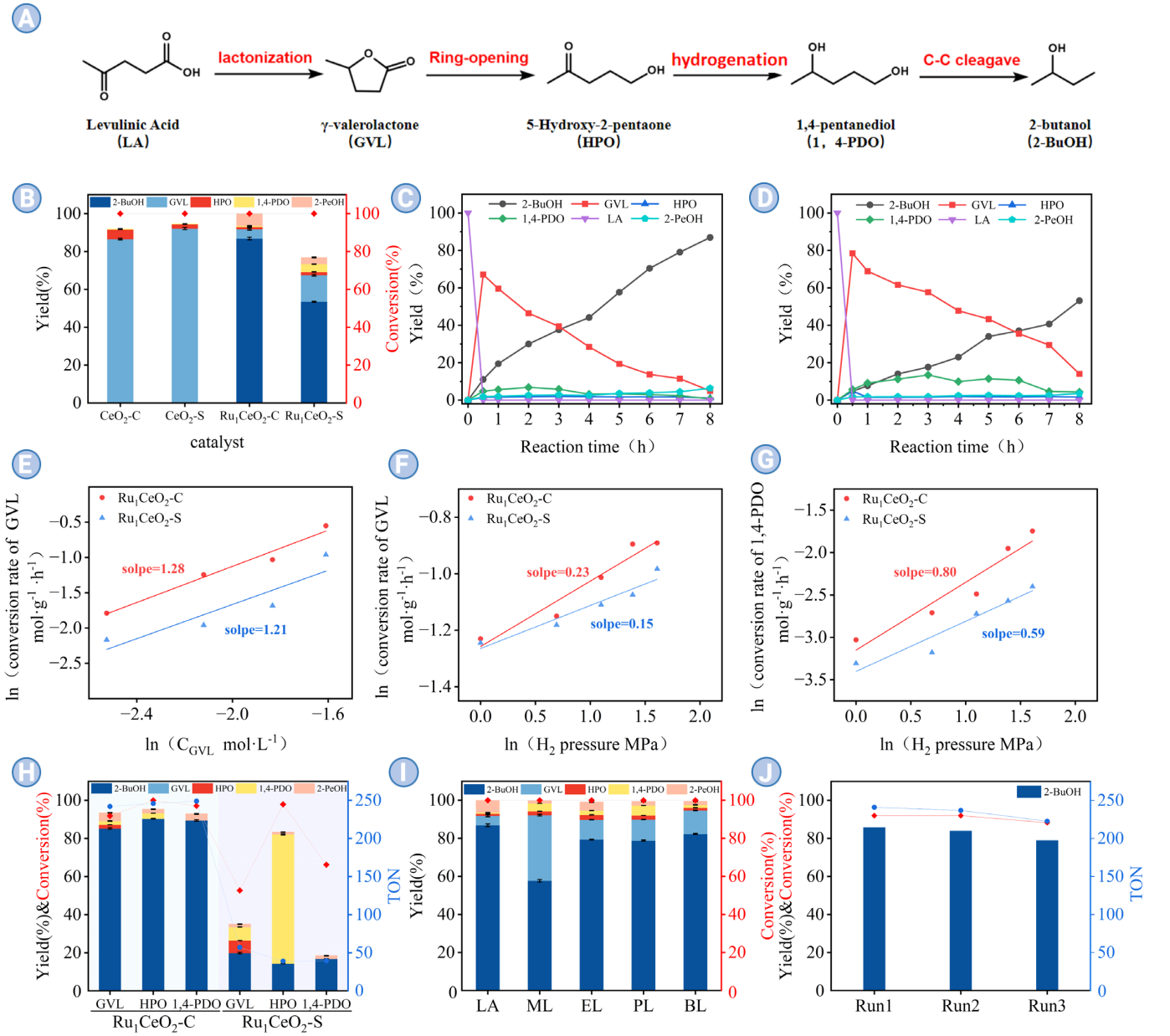

Figure 4. (A) Proposed reaction pathway for LA hydrodeoxygenation to 2-butanol. (B) Conversion of LA over different catalysts. Time evolution of product distributions in LA hydrodeoxygenation over (C) Ru_1CeO_2-C and (D) Ru_1CeO_2-S catalysts. Determination of apparent reaction orders with respect to (E) GVL concentration and (F) H_2 pressure during GVL hydrodeoxygenation. (G) Apparent reaction orders with respect to H_2 pressure in 1,4-PDO hydrodeoxygenation. (H) Catalytic activity of Ru_1CeO_2-C and Ru_1CeO_2-S for the conversion of key reaction intermediates. (I) Substrate scope evaluation: catalytic conversion of various levulinates over Ru_1CeO_2-C. (J) Recycling tests of Ru_1CeO_2-C in the catalytic GVL hydrodeoxygenation (Reaction conditions: 0.07 g catalyst, 0.14 g GVL, 8.65 mL IPA, 190 °C, 5 MPa H_2, and 8 h).

shows a hydrogen donor with the product of acetone observed, enabling partial hydrogenation of LA to form GVL, while no further hydrogenolysis products were observed, suggesting IPA alone is not sufficient to drive the deep hydrodeoxygenation pathway (Figure S3). Nonetheless, the effect of solvents shows that IPA presents the best catalytic performance than other solvents (ethanol, methanol, and water).

To elucidate the deactivation mechanism of the catalyst during the key reaction step and evaluate its structural stability in this step, the recyclability of Ru_1CeO_2-C was evaluated in the hydrogenolysis of GVL (Figure 4J). After three consecutive cycles, only a slight decline in activity was observed, with GVL conversion remaining above 88% and 2-butanol yield above 78%. To elucidate the causes of performance loss, the spent catalyst was characterized using XPS, TGA, SEM, and Raman spectroscopy (Figure S4 & Table S4). XPS analysis reveals a decrease in Ce^{3+} and O_β contents, accompanied by a decrease in the $Ru^{\delta+}/(Ru^{\delta+} + Ru^0)$ ratio. Raman spectra further show weakened Ru-O-Ce characteristic bands (~693 and ~978 cm^{-1}), indicating attenuation of metal–support interactions. TGA analysis shows that the spent Ru_1CeO_2-C catalyst exhibits approximately 5% greater weight loss compared to the fresh catalyst, probably due to the adsorbed acetone or coke formation [7]. Meanwhile, SEM images reveal that the spent catalyst is fragmented into smaller particles. These observations together contribute to the observed slight loss of catalytic activity. Overall, these results demonstrate that Ru_1CeO_2-C combines high activity, selectivity, and reasonable stability for LA hydrodeoxygenation.

Reaction mechanism

During the conversion of LA to 2-butanol, LA is rapidly hydrogenated to GVL, and the subsequent hydrodeoxygenation of GVL is identified as the key rate-determining step. As shown in Figure 5A, Ru_1CeO_2-C exhibits a significantly higher catalytic efficiency than Ru_1CeO_2-S, with a TON of 208 and a TOF of 157 s^{-1}, compared with TON = 129 and TOF = 111 s^{-1} for Ru_1CeO_2-S. The kinetics of GVL hydrogenolysis study show yield apparent activation

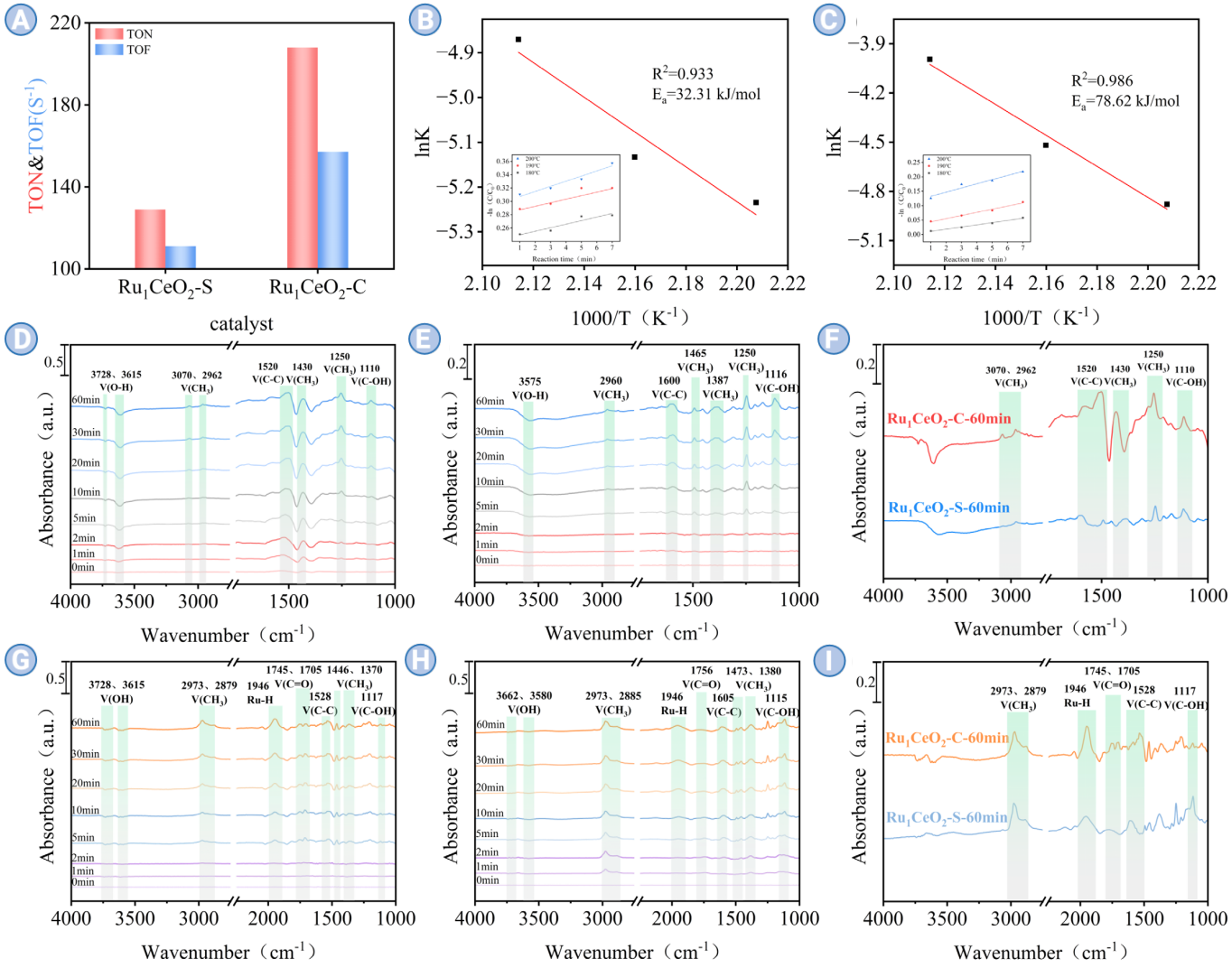

Figure 5. (A) Comparison of TON and TOF for Ru_1CeO_2-C and Ru_1CeO_2-S catalysts in LA hydrodeoxygenation. Apparent activation energy of (B) Ru_1CeO_2-C and (C) Ru_1CeO_2-S catalysts in GVL hydrodeoxygenation. *In situ* DRIFTS of the interaction/reaction (D) between Ru_1CeO_2-C and 1,4-PDO, (E) between Ru_1CeO_2-S and 1,4-PDO, (F) between catalysts and 1,4-PDO at 60 min, (Gg) between IPA and Ru_1CeO_2-C, (H) between IPA and Ru_1CeO_2-S, and (I) between catalysts and IPA at 60 min.

energies of 32.31 kJ mol^{-1} for Ru_1CeO_2-C and 78.62 kJ mol^{-1} for Ru_1CeO_2-S, demonstrating a substantially lower energy barrier on the cubic catalyst (Figure 5B&C). Moreover, the apparent activation energies for the conversion of key intermediates, including 1,4-PDO and HPO, are consistently lower on Ru_1CeO_2-C than on Ru_1CeO_2-S (Figure S4). These results indicate that Ru_1CeO_2-C more effectively activates GVL and its downstream intermediates, thereby enabling the highest 2-butanol yield. For both catalysts, GVL hydrogenolysis showed highest apparent activation energy than hydrogenolysis of other substrates, suggesting rate-determining step of GVL hydrogenolysis in the LA hydrodeoxygenation to 2-butanol in this system.

To further elucidate the facet-dependent reaction mechanism, *in situ* DRIFTS was employed to probe the interaction between Ru_1CeO_2 catalysts and 1,4-PDO (Figure 5D-F). As shown in Figure 5D, the DRIFTS spectra of the interaction between Ru_1CeO_2-C and 1,4-PDO adsorption exhibit progressively increasing intensities of $\nu(CH_3)$ bands at ~3079, 2962, 1430, and 1250 cm^{-1}, as well as a ν(C-C) band at ~1520 cm^{-1}, indicating strong adsorption and activation of carbon–carbon bonds on the Ru_1CeO_2-C surface.[48] Concurrently, the appearance of a ν(C-OH) band at ~1100 cm^{-1}, characteristic of secondary alcohols,[49] confirms that this interaction promotes selective C-C bond cleavage in 1,4-PDO, leading to the formation of 2-butanol. In contrast, Ru_1CeO_2-S shows much weaker ν(C-C) and ν(C-H) signals during 1,4-PDO adsorption (Figure 5E), indicating limited activation of the C-C bond. On the bare CeO_2-C support, these characteristic features are almost undetectable (Figure S5), confirming the indispensable role of Ru single atoms. A direct comparison of spectra collected after 60 min (Figure 5F) clearly demonstrates that the CeO_2(1 0 0) facet exposed in Ru_1CeO_2-C strongly promotes the C–C bond cleavage pathway of 1,4-PDO toward 2-butanol formation.

The hydrogen transfer ability of the catalyst was further verified by *in situ* DRIFTS experiments on the interaction between IPA and the catalyst (Figure 5G-I). With increasing interaction time, both Ru_1CeO_2-C and Ru_1CeO_2-S display prominent $\nu(CH_3)$ bands at ~2973, 2879, 1466, and 1270 cm^{-1} and a ν(C-C) band at ~1520 cm^{-1}, confirming effective interaction/reaction of IPA on both surfaces.[7] However, Ru_1CeO_2-C exhibits significantly stronger bands corresponding to Ru–H species (~1946 cm^{-1}) and carbonyl (C=O) stretching (~1720 cm^{-1}) compared with Ru_1CeO_2-S.[50] Meanwhile, the ν(C-OH) band of secondary alcohols at ~1117 cm^{-1} is markedly weaker on Ru_1CeO_2-C, indicating faster dehydrogenation of IPA to acetone. These observations demonstrate that Ru_1CeO_2-C possesses superior hydrogen-transfer activity, enabling more efficient generation of reactive hydrogen species. A direct comparison of DRIFTS spectra after 60 min (Figure 5I) further corroborates the enhanced hydrogen-transfer capability of Ru_1CeO_2-C. In contrast, only IPA adsorption features are observed on the CeO_2-C support, while Ru–H and C=O signals are entirely absent (Figure S5), underscoring the crucial role of Ru single atoms in IPA activation.

Collectively, these results demonstrate that the CeO_2(1 0 0) facet, enriched with oxygen vacancies and strong Ru-O-Ce interfacial structures, synergistically enhances both hydrogen transfer and C-C bond cleavage. This facet-dependent regulation of electronic structure and adsorption behavior

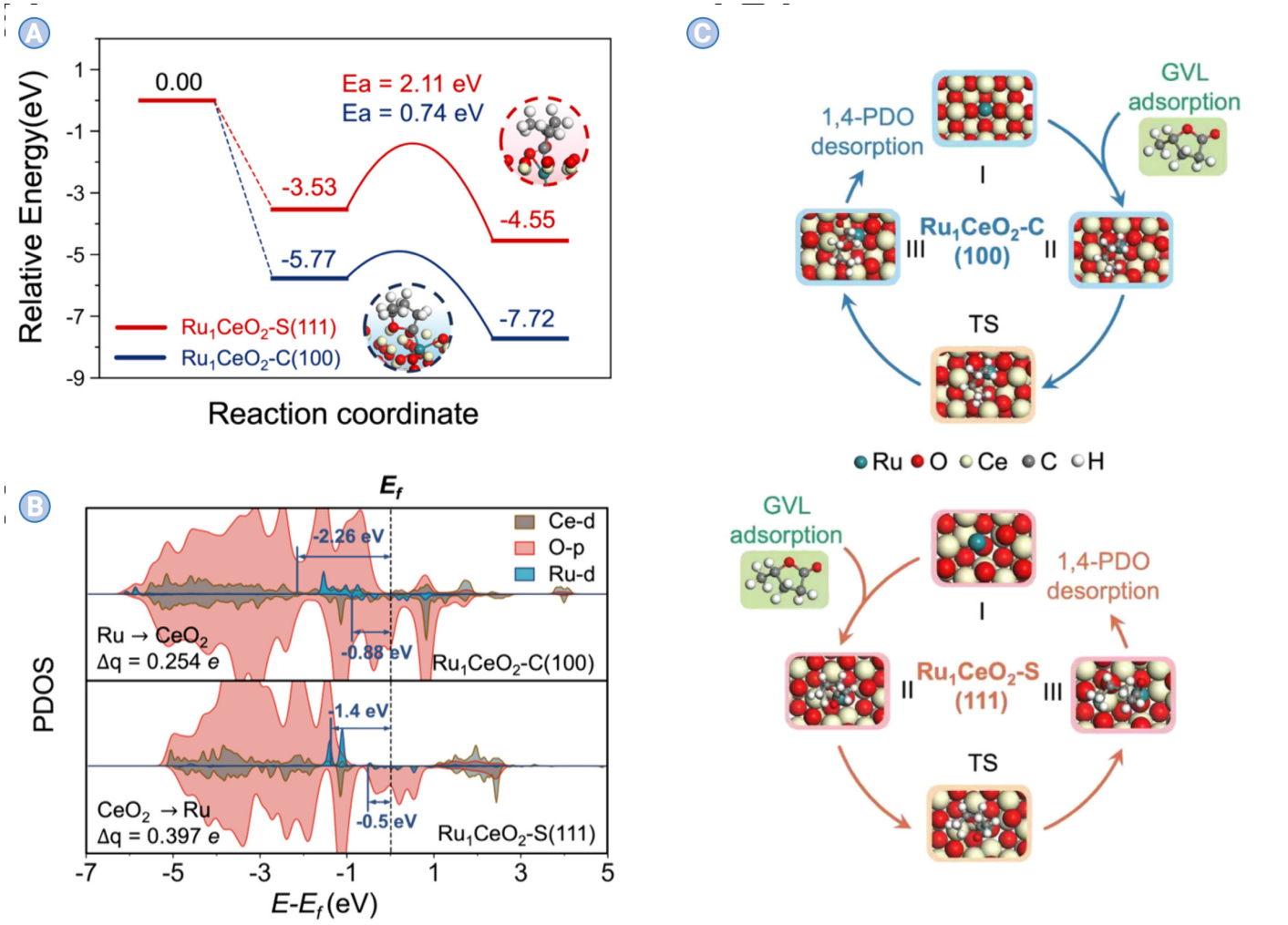

Figure 6. (A) Calculated energy profiles for GVL ring-opening reaction on Ru_1CeO_2-C (100) and Ru_1CeO_2-S (111) surfaces. (B) Projected density of state (PDOS) for Ru_1CeO_2 catalysts and electron transfer analysis. (C) Optimized geometric configurations for GVL-ring-opening reactions.

accounts for the superior activity and selectivity of Ru_1CeO_2-C toward 2-butanol formation from levulinic acid.

Structure-activity relationship

This study demonstrates that facet engineering of Ru_1CeO_2 catalysts via interfacial structure regulation provides an effective strategy to tune catalytic performance in the hydrogenation of LA to 2-butanol. Systematic characterization of the catalyst structure, physicochemical properties, and catalytic behavior reveals a strong correlation between exposed CeO_2 crystal facets and reaction performance.

XPS, EPR, and Py-FTIR analyses collectively show that Ru_1CeO_2-C, which predominantly exposes the CeO_2(1 0 0) facet, possesses a significantly higher concentration of surface oxygen vacancies than Ru_1CeO_2-S with exposed CeO_2(1 1 1) facets. Moreover, Ru single atoms preferentially form Ru-O-Ce interfacial structures on the CeO_2-C surface, leading to EMSI. This interfacial configuration stabilizes Ru predominantly in the oxidation state and generates synergistically enhanced Lewis acid sites near oxygen vacancies. The coexistence of abundant oxygen vacancies and Lewis acid sites effectively promote the rate-determining hydrocracking step of LA, the ring-opening of GVL, which is corroborated by the markedly different GVL conversion kinetics observed for Ru_1CeO_2-C and Ru_1CeO_2-S. In addition to enhanced Lewis acidity, *in situ* DRIFTS analyses reveal that Ru_1CeO_2-C exhibits superior hydrogen-transfer capability, enabling more efficient activation of hydrogen donor molecules and facilitating subsequent hydrogenolysis steps. This dual functionality—strong Lewis acidity for C–O/C–C bond activation and efficient hydrogen transfer for hydrogenation—accounts for the superior activity and selectivity of Ru_1CeO_2-C toward 2-butanol formation.

DFT calculations further substantiate the experimentally observed facet-dependent activity (Figure 6). As shown in Figure 6A, the ring-opening of GVL, identified as the rate-determining step in LA hydrodeoxygenation, proceeds with a substantially lower activation barrier on the Ru_1CeO_2-C(100) (E_a = 0.74 eV) than on the Ru_1CeO_2-S(111) (E_a = 2.11 eV), confirming the intrinsically higher reactivity of the (1 0 0) facet. In addition, GVL adsorption on Ru_1CeO_2-C(100) is significantly stronger than on Ru_1CeO_2-S(111), as reflected by the more negative adsorption energy (-5.77 vs -3.53 eV), indicating a higher affinity between the reactant and the catalytically active surface. Charge-density difference analysis (Figure 6B) reveals distinct facet-dependent electronic interactions. On Ru_1CeO_2-C(100), the Ru single atom donates 0.254 |e| to the CeO_2(1 0 0) support, whereas on Ru_1CeO_2-S(111), the CeO_2(1 1 1) surface transfers 0.397 |e| to the Ru atom. These opposite electron-transfer behaviors are consistent with the XPS-derived Ru oxidation states and confirm that facet-dependent electronic modulation governs the strength of Ru-O-Ce interactions.

CONCLUSION

In summary, this study demonstrates that the catalytic performance of single-atom Ru_1CeO_2 catalysts for the hydrodeoxygenation of levulinic acid to 2-butanol is profoundly influenced by the crystal facets of the ceria support. By anchoring Ru single atom species onto cubic CeO_2-C (1 0 0) and sheet-like CeO_2-S (1 1 1) supports via photodeposition, we identified that the (1 0 0) facets facilitate a higher concentration of surface oxygen vacancies and foster the electronic metal-support interaction. These structural features significantly enhance the abundance of Lewis acid sites and improve hydrogen transfer efficiency, leading to a superior 2-butanol yield of 86.9% and a

TOF of 157 s^{-1} over the Ru_1CeO_2-C catalyst. These findings provide critical insights into facet-directed interfacial engineering for the design of high-performance single-atom catalysts in sustainable biomass valorization.

REFERENCES

1. Liu Y., Chen L.A., Chen Y.B., et al. (2023). Pilot study on production of aviation fuel from catalytic conversion of corn stover. *Bioresour. Technol.* **372**:128653. DOI:10.1016/j.biortech.2023.128653
2. Liao Y., Koelewijn S.-F., Van den Bossche G., et al. (2020). A sustainable wood biorefinery for low–carbon footprint chemicals production. *Science* **367**:1385–1390. DOI:10.1126/science.aau1567
3. Singhawat K., Thubsuang U., Saramolee P., et al. (2025). Fractionation of palm oil empty fruit bunch using deep eutectic solvent for lignin recovery and cellulose conversion to levulinic acid. *Biomass Bioenergy* **202**:108184. DOI:10.1016/j.biombioe.2025.108184
4. Chen Z., Wu Y., Huang J.H., et al. (2015). Metabolic engineering of Klebsiella pneumoniae for the de novo production of 2-butanol as a potential biofuel. *Bioresour. Technol.* **197**:260–265. DOI:10.1016/j.biortech.2015.08.086
5. Rao T.U., Suchada S., Choi C., et al. (2022). Selective hydrogenation of furfural to tetrahydrofurfuryl alcohol in 2-butanol over Ni–Cu–Al catalyst. *Energy Convers. Manage.* **265**:115736. DOI:10.1016/j.enconman.2022.115736
6. Chen L.G., Liu Y., Gu C.S., et al. (2021). Selective production of 2-butanol from hydrogenolysis of levulinic acid catalyzed by NiMn bimetallic catalyst. *ACS Sustain. Chem. Eng.* **9**:15603–15611. DOI:10.1021/acssuschemeng.1c05771
7. Gao L.L., Long Y.W., Xiao Z.G., et al. (2025). Synergistic regulation of oxygen vacancy and Lewis acid sites by Ru loading for boosting 2-butanol production. *J. Catal.* **450**:116302. DOI:10.1016/j.jcat.2025.116302
8. Lv J.K., Rong Z.M., Sun L.M., et al. (2018). Catalytic conversion of biomass-derived levulinic acid into alcohols over nanoporous Ru catalyst. *Catal. Sci. Technol.* **8**:975–979. DOI:10.1039/c7cy01838j
9. Mizugaki T., Togo K., Maeno Z., et al. (2017). New routes for refinery of biogenic platform chemicals catalyzed by CeO2-supported Ru nanoparticles. *Sci. Rep.* **7**:14007. DOI:10.1038/s41598-017-14373-1
10. Liu Y., Gu C.S., Chen L.G., et al. (2023). Ru–MnOx interaction for efficient hydrodeoxygenation of levulinic acid and derivatives. *ACS Appl. Mater. Interfaces* **15**:4184–4193. DOI:10.1021/acsami.2c22045
11. Zhang Y., Zhao S., Feng J., et al. (2021). Physical chemistry and materials science of CeO2-based nanostructures. *Chem* **7**:2022–2059. DOI:10.1016/j.chempr.2021.02.015
12. Grabchenko M.V., Mamontov G.V., Zaikovskii V.I., et al. (2020). Metal-support interaction in Ag/CeO2 catalysts. *Appl. Catal. B: Environ.* **260**:118148. DOI:10.1016/j.apcatb.2019.118148
13. Fang Y., He Y., Liu K., et al. (2025). Ceria facet engineering and Mo-modified acidity in Pt/CeO2 catalysts. *J. Rare Earths*. DOI:10.1016/j.jre.2025.12.017.
14. Mao L.T., Song Z.X., Fan J., et al. (2025). Role of oxygen vacancies on ceria crystal planes. *Sep. Purif. Technol.* **360**:131131. DOI:10.1016/j.seppur.2024.131131
15. Zhang L.J., Chen R.H., Tu Y., et al. (2023). Crystal facet effect of ceria in Pd/CeO2 catalysts. *ACS Catal.* **13**:2202–2213. DOI:10.1021/acscatal.2c04252
16. Trovarelli A. and Llorca J. (2017). Ceria catalysts at nanoscale. *ACS Catal.* **7**:4716–4735. DOI:10.1021/acscatal.7b01246
17. Tong T., Liu X.H., Guo Y., et al. (2018). Role of CeO2 crystal plane in controlling Pt states. *J. Catal.* **365**:420–428. DOI:10.1016/j.jcat.2018.07.023
18. Mai H.X., Sun L.D., Zhang Y.W., et al. (2005). Shape-selective synthesis and oxygen storage of ceria nanostructures. *J. Phys. Chem. B* **109**:24380–24385. DOI:10.1021/jp055584b
19. Dai Q.G., Bai S.X., Li H., et al. (2014). Synthesis of CeO2 nanosheets via aqueous precipitation. *CrystEngComm* **16**:9817–9827. DOI:10.1039/c4ce01436g
20. Esther Jeyanthi C., Karnan C., Kistan A., et al. (2023). Cobalt doping effects in CeO2 ceramics. *Inorg. Chem. Commun.* **153**:110836. DOI:10.1016/j.inoche.2023.110836
21. Gao Y.X., Zhang Z.H., Li Z.R., et al. (2020). Morphology-dependent CuOx–CeO2 interaction. *Chin. J. Catal.* **41**:1006–1016. DOI:10.1016/S1872-2067(19)63503-5
22. Xie X.L., Wang J.R., Guo X.C., et al. (2024). CeO2 catalysts with different morphologies for ozonation. *J. Colloid Interface Sci.* **673**:847–859. DOI:10.1016/j.jcis.2024.06.119
23. Busch I., Liu W.D., Chen C., et al. (2017). Ellipsometry for oxide layer measurement. *Appl. Surf. Sci.* **421**:624–629. DOI:10.1016/j.apsusc.2017.01.125
24. Caddeo F., Casu A., Loche D., et al. (2021). Thermally stable ceria nanocubes. *J. Colloid Interface Sci.* **583**:376–384. DOI:10.1016/j.jcis.2020.09.044
25. Ziemba M., Weyel J. and Hess C. (2022). Operando study on Cu/CeO2 catalysts. *ACS Catal.* **12**:9503–9514. DOI:10.1021/acscatal.2c02216
26. Fang Y.F., Han X.Y., Liu K.J., et al. (2026). Dual-atom catalyst for propane combustion. *Nat. Chem.* DOI:10.1038/s41557-025-02062-w.
27. Gao X., Huang G., Jing S., et al. (2025). Strategies for single-atom catalysts in ORR. *Innov. Mater.* **3**:100141. DOI:10.59717/j.xinn-mater.2025.100141
28. Long J.R., Mao Y.X., Long Y.W., et al. (2026). Ru/HZSM-5 for hydrodeoxygenation of lignin phenols. *Bioresour. Technol.* **439**:133357. DOI:10.1016/j.biortech.2025.133357
29. Wang Y.F. and Wang R.G. (2022). CeO2 nanorods supported Ru catalysts. *J. Colloid Interface Sci.* **613**:836–846. DOI:10.1016/j.jcis.2022.01.062
30. Li J.H., Liu Z.Q., Cullen D.A., et al. (2019). Distribution of Ru species on CeO2 supports. *ACS Catal.* **9**:11088–11103. DOI:10.1021/acscatal.9b03113
31. Ren G.M., Chen X.Y., Zhao Z.H., et al. (2025). Photocatalytic C–N coupling on Ru single atoms. *Adv. Funct. Mater.* **35**:2506296. DOI:10.1002/adfm.202506296
32. Zhu Y.C., Li C.T., Liang C.X., et al. (2023). CeO2 morphology and catalytic oxidation of toluene. *J. Catal.* **418**:151–162. DOI:10.1016/j.jcat.2023.01.012
33. Long G.C., Wang A.D., Liu X., et al. (2025). Oxygen vacancy clusters in CeO2 nanorods. *Angew. Chem. Int. Ed.* **64**:e202508217. DOI:10.1002/anie.202508217
34. Hu Z., Liu X.F., Meng D.M., et al. (2016). Effect of ceria crystal plane on Pd/CeO2. *ACS Catal.* **6**:2265–2279. DOI:10.1021/acscatal.5b02617
35. Nolan M., Parker S.C. and Watson G.W. (2005). Electronic structure of oxygen vacancy defects in ceria. *Surf. Sci.* **595**:223–232. DOI:10.1016/j.susc.2005.08.015
36. Huang M. and Fabris S. (2008). CO adsorption and oxidation on ceria surfaces. *J. Phys. Chem. C* **112**:8643–8648. DOI:10.1021/jp709898r
37. Zhang K., Meng Q., Wu H., et al. (2022). Selective hydrodeoxygenation over Ru single atoms on CeO2. *J. Am. Chem. Soc.* **144**:20834–20846. DOI:10.1021/jacs.2c08992
38. Tao S.Y., Wang X., Rao C., et al. (2026). Pd–Ce diatomic interaction for methane oxidation. *Adv. Funct. Mater.* **36**. DOI:10.1002/adfm.202519202.
39. Zhang X., Zhou Y. and Xing M. (2026). Environmental catalysts with high activity and stability. *Innov. Mater.* **4**:100166. DOI:10.59717/j.xinn-mater.2025.100166
40. Dai Q.G., Huang H., Zhu Y., et al. (2012). Catalytic oxidation over ceria nanocrystals. *Appl. Catal. B: Environ.* **117**:360–368. DOI:10.1016/j.apcatb.2012.02.001
41. Weber W.H., Hass K.C. and McBride J.R. (1993). Raman study of CeO2. *Phys. Rev. B* **48**:178–185. DOI:10.1103/PhysRevB.48.178
42. Zhang B.F., Yang J.W., Mu Y.B., et al. (2024). Highly dispersed Ru catalysts on CeO2. *Environ. Sci. Technol.* **58**:19533–19544. DOI:10.1021/acs.est.4c07159
43. Sivan S.E., Kang K.H., Han S.J., et al. (2022). MOF-derived Ru catalysts on CeO2. *J. Catal.* **408**:316–328. DOI:10.1016/j.jcat.2022.03.019
44. Liu Y., Long J.R., Huang Z.J., et al. (2024). Production of HMF and DMF from fructose. *Biomass Bioenergy* **190**:107405. DOI:10.1016/j.biombioe.2024.107405
45. Luo S., Mao M., Yu H., et al. (2024). Oxygen vacancy regulation for glucose conversion. *Catal. Today* **434**:114709. DOI:10.1016/j.cattod.2024.114709
46. Joshi N., Gawas P., Bora A., et al. (2023). Zeolite for gas sensing of VOCs. *Surf. Interfaces* **42**:103364. DOI:10.1016/j.surfin.2023.103364
47. Wang J.F., Lu X.B., Wang Y.Y., et al. (2025). Ru-based nanoreactors for biomass conversion. *ACS Catal.* **15**:9266–9276. DOI:10.1021/acscatal.4c08089
48. Ye S.J., Lian X.Y., Liu B.Y., et al. (2023). Deep oxidation of toluene. *Appl. Catal. B: Environ.* **334**:122802. DOI:10.1016/j.apcatb.2023.122802
49. Wang J.M., Zhu S.H., He Y., et al. (2024). Pt/Mg–Al catalysts for hydrogenation. *Catal. Today* **433**:114647. DOI:10.1016/j.cattod.2024.114647
50. Zhang P., Sui X.Y., Wang Y., et al. (2023). Ru-based nanohybrids for CO_2 methanation. *J. Am. Chem. Soc.* **145**:5769–5777. DOI:10.1021/jacs.2c12632

FUNDING AND ACKNOWLEDGMENTS

The authors acknowledge the support from the National Natural Science Foundation of China (52466017 and 22479024), the Natural Science Foundation of Jiangxi Province (20242BAB25277), and a Talent Program of Jiangxi Province of China grant No. jxsq2020102023. The authors also thank the Beijng PARATERA Tech CO., Ltd. for providing HPC resources that have contributed to the research results.

AUTHOR CONTRIBUTIONS

Zhang Shaohua: Investigation. Liu Fusen: Writing – original draft, Validation, Investigation, Data curation. Zhang Yuqi: Investigation. Zhou Wenguang: Resources, Formal Analysis. Chen Lungang: Visualization, Formal Analysis. Liu Yong: Writing – review & editing, Supervision, Software, Resources, Methodology, Investigation, Funding acquisition, Conceptualization. All authors contributed to the manuscript and approved the final version.

DECLARATION OF INTERESTS

The authors declare no competing interests.

DATA AND CODE AVAILABILITY

Data are available from the corresponding author upon reasonable request.

SUPPLEMENTAL INFORMATION

It can be found online at: https://doi.org/10.59717/j.xinn-energy.2026.100156